European Journal of Mechanics / B Fluids 79 (2020) 255–269

Contents lists available at ScienceDirect

European Journal of Mechanics / B Fluids

journal homepage: www.elsevier.com/locate/ejmflu

Vortex dynamics and flow patterns in a two-dimensional oscillatory lid-driven rectangular cavity

Jianxun Zhu *, Lars Erik Holmedal, Hong Wang, Dag Myrhaug

Department of Marine Technology, Norwegian University of Science and Technology, Trondheim, Norway

ARTICLE INFO

Article history:
Received 5 March 2019
Received in revised form 16 September 2019
Accepted 17 September 2019
Available online 21 September 2019

Keywords:
Vortex dynamics
Oscillatory lid-driven cavity flow

ABSTRACT

The vortex dynamics in a two-dimensional oscillatory lid-driven cavity with depth-to-width ratio 1:2 has been investigated, covering a wide range of Reynolds numbers and Stokes numbers where this flow is known to be in the two-dimensional regime. Numerical simulations show that the present flow can be divided into four flow patterns based on the vortex dynamics. The regions of these flow patterns are given in the Stokes number and Reynolds number space. For the flow pattern with lowest Reynolds number, there is no transfer of vortices between two successive oscillation half-cycles while for the three other patterns, vortices are carried over from one oscillation half-cycle to the next. For a given Stokes number, the flow pattern appears sequentially as the Reynolds number increases, showing that the transition between the different flow patterns depends strongly on the Reynolds number. However, if the frequency of oscillation is increased (i.e., the Stokes number is increased) for a given Reynolds number, the extrema of the stream function have less time to grow and the center of the primary vortex has less time to move away from the lid. To compensate these effects, the amplitude has to be increased with increasing frequency to maintain the same flow pattern.

1. Introduction

Flow in an oscillatory lid-driven cavity has been studied over the years because of its relevance to industrial flows. Despite the simple geometry involved, this flow contains several complex hydrodynamic flow structures and phenomena, such as vortex merging [1,2], flow separation [3,4], corner singularities [5,6], boundary layers [7,8] and chaotic mixing [9,10]. Comprehensive reviews of lid-driven cavity flows are given by Shankar and Deshpande [5] and by Kuhlmann and Romanò [11]. Oscillatory lid-driven cavity flows are characterized by a Stokes layer beneath the horizontally oscillating lid which rolls up at the vertical side walls, forming one clockwise and one anti-clockwise primary vortex which alternate in growing and decaying during the oscillation cycle. Flow separation leads to the formation and evolution of corner vortices which in turn interacts with the primary vortices, thus exhibiting a complicated vortex dynamics, as shown by Soh and Goodrich [12], Iwatsu et al. [13] and Mendu and Das [14] for square cavities.

Ovando et al. [15] used numerical simulations to investigate the flow in a rectangular cavity driven by a simultaneous oscillatory motion of the vertical walls, relevant to a piston moving inside a circular cylinder in combustion engines. They found two major generation mechanisms for the primary vortex: (*i*) vorticity produced by the shear motion induced by the oscillating walls, and (*ii*) roll-up of vortex sheets as the wall-induced flow changes direction when the fluid meets the vertical walls, as previously observed in experiments by Tabaczynski et al. [16] and Allen and Chong [17].

The possible application of an oscillatory lid-driven cavity flow as a viable viscometer [18] spurred further investigations of the stability of the two-dimensional base flow, including the experimental work by Vogel et al. [19] and Leung et al. [20] and the stability analysis by Blackburn and Lopez [21]. These works resulted in stability regions as a function of the Reynolds number *Re* (based on the height of the cavity and the oscillation velocity amplitude of the lid) and the Stokes number *St* (based on the height of the cavity and the oscillation frequency of the lid). Three different flow states were found: (*i*) a basic two-dimensional time-periodic flow, (*ii*) a three-dimensional time-periodic flow with a cellular structure in the spanwise direction, (*iii*) a three-dimensional irregular flow.

The vortex dynamics for two-dimensional oscillatory lid-driven cavity flows is more complex than for steady lid-driven cavity flows [4,22] as it includes the evolution of intermediate primary and secondary vortices through the oscillation cycle, where the location and duration of these intermediate vortices depend strongly on the Reynolds number and the Stokes number. The aim of the present paper is to provide a further detailed investigation of the vortex dynamics for an oscillatory lid-driven

* Corresponding author.
E-mail address: jianxun.zhu@ntnu.no (J. Zhu).

https://doi.org/10.1016/j.euromechflu.2019.09.013

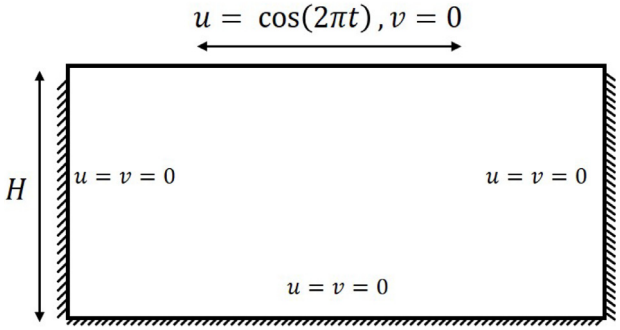

Fig. 1. Sketch for the oscillatory lid-driven rectangular cavity flow.

cavity with depth-to-width ratio 1:2, covering the wide range of the Reynolds number and the Stokes number where this flow is known to be in the two-dimensional regime [19]. Numerical simulations show that this flow regime can be further divided into four different flow patterns based on the vortex dynamics, which is visualized by instantaneous streamline contours through the first half-cycle of oscillation. These flow patterns are mapped out in the Stokes number and Reynolds number space, and a detailed analysis of the vortex dynamics underpinning the flow pattern classification is presented, including the interaction between the primary vortices and the corner and wall vortices, which has not been previously investigated in such detail.

2. Governing equations

Incompressible flow with a constant density ρ and kinematic viscosity ν is governed by the two-dimensional Navier–Stokes equations described as follows

$$\frac{\partial u_i}{\partial x_i} = 0 \tag{1}$$

$$\frac{St}{Re}\frac{\partial u_i}{\partial t} + \frac{\partial u_i u_j}{\partial x_j} = -\frac{\partial p}{\partial x_i} + \frac{1}{Re}\frac{\partial^2 u_i}{\partial x_j \partial x_j} \tag{2}$$

where the Einstein notation using repeated indices is applied. Here $u_i = (u, v)$ and $x_i = (x, y)$ for $i = 1$ and 2, are the velocity and Cartesian coordinates, respectively, whilst t, p, $Re = U_0 H/\nu$ and $St = \omega H^2/\nu$ denote the time, pressure, Reynolds number and Stokes number, respectively, where H, U_0 and ω are the depth of the cavity, the velocity amplitude of the lid motion and the oscillation frequency of the lid, respectively. The velocity, time, pressure and length are scaled with U_0, T, ρU_0^2 and H, respectively, where T is the period of the lid oscillation. Fig. 1 shows a sketch of the oscillatory lid-driven cavity. The velocity of the lid is given by $u = cos(2\pi t)$ while no-slip conditions are imposed on the side and bottom walls.

3. Numerical method

Eqs. (1) and (2) have been solved by using a projection method with a semi-implicit time integration using a second-order Adams–Bashforth scheme for the convective terms and a Crank–Nicolson scheme for the diffusive terms. Second-order central differences with a staggered grid arrangement are applied in the spatial discretization. The intermediate velocity u_i^* is obtained as

$$u_i^* = u_i^n + \Delta t[\frac{1}{2}(3H_i^n - H_i^{n-1}) + \frac{1}{2}(F_i^n + F_i^*) - \frac{1}{Re}\frac{\delta}{\delta x_i}(p^{n-1/2})] \tag{3}$$

where $\delta/\delta x_i$ represents the numerical spatial gradient operator; the convective and diffusive terms are denoted by $H_i = \delta(u_i u_j)/\delta x_j$ and $F_i = \nu\delta^2(u_i)/(\delta x_j \delta x_j)$, respectively; the superscript n denotes the time step, and $p^{n-1/2}$ indicates the pressure obtained at the previous time-step. The velocity correction is

$$u_i^{n+1} = u_i^* - \Delta t\frac{\delta}{\delta x_j}(\phi^{n+1}) \tag{4}$$

where $\phi^{n+1} = p^{n+1/2} - p^{n-1/2}$ is determined such that the resulting velocity field u_i^{n+1} satisfies the continuity condition. Substitution of Eq. (4) into the continuity equation $\delta u_i/\delta x_i = 0$ yields a Poisson equation for the pressure correction

$$\frac{\delta^2}{\delta x_j^2}(\phi^{n+1}) = -\frac{1}{\Delta t}\frac{\delta u_i^*}{\delta x_i} \tag{5}$$

where Neumann conditions are applied for the pressure corrections on all the walls and on the lid.

The oscillatory lid-driven cavity flow starts from rest, and after a spin-up time of typically 6–16 cycles (depending on Re and St), the flow reaches a fully-developed periodic state, i.e. where the velocity and pressure fields at t and $t + T$ are equal within a specified numerical accuracy. The criterion for the flow being fully-developed is given by

$$max|\frac{u_i(x, y, t + T) - u_i(x, y, t)}{u_i(x, y, t + T)}| \le \varepsilon, \quad i = 1, 2 \tag{6}$$

where $\varepsilon = 1 \times 10^{-6}$.

Based on grid convergence tests, a spatial resolution of 100×100 and 100×200 uniform grid points is sufficient to obtain grid independent results, for the depth-to-width ratios 1:1 and 1:2, respectively.

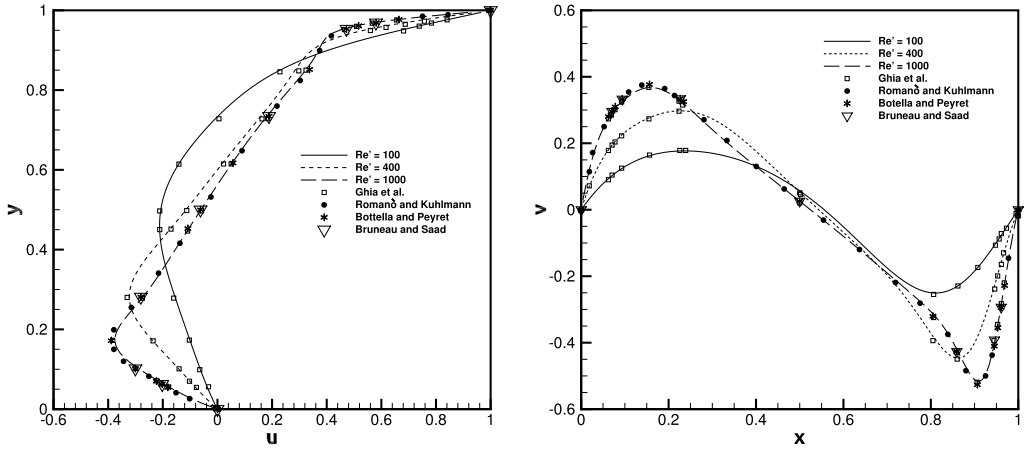

Fig. 2. Comparisons of $u(0.5, y)$ and $v(x, 0.5)$ between predictions and reference data for the steady lid-driven cavity flow with $Re' = 100$, 400 from Ghia et al. [22] and $Re' = 1000$ from Ghia et al. [22], Romanò and Kuhlmann [23], Bottella and Peyret [24] and Bruneau and Saad [25].

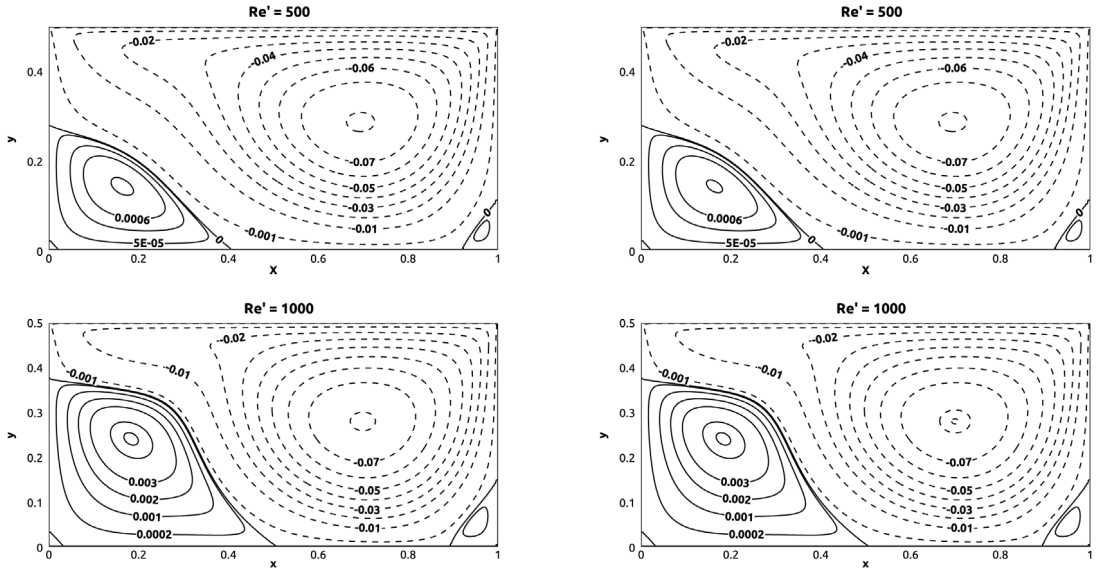

Fig. 3. Streamline contours for $Re' = 500$ and 1000. Present results (left) and the results by Cheng and Hung [4] (right) which were digitalized.

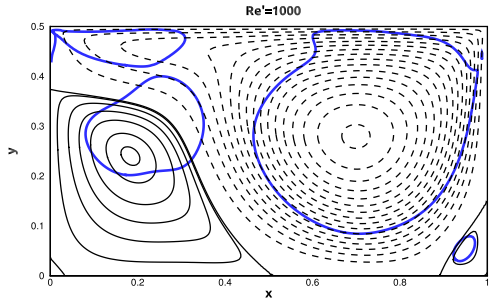

Fig. 4. Streamlines (positive values for black full lines; negative values for black dashed lines) and $\lambda_2 = -0.1$ (blue lines) contours for steady lid-driven rectangular cavity flow at $Re' = 1000$.

4. Validation against previous numerical and experimental results

4.1. Steady lid-driven cavity flow

Fig. 2 shows the center-line velocities $u(0.5, y)$ and $v(x, 0.5)$ for a steady lid-driven flow in a square cavity for $Re' = UH/\nu = 100$, 400 and 1000, where U is the constant lid velocity. The velocity gradients near the wall increase as Re' increases, and the thickness of the boundary layers at the wall decreases as Re' increases. A good agreement is obtained with the results by Ghia et al. [22] for $Re' = 100$, 400 and 1000 and by Romanò and Kuhlmann [23], Bottella and Peyret [24] and Bruneau and Saad [25]. for $Re' = 1000$.

Fig. 3 shows the streamlines for a steady lid-driven flow in a rectangular cavity with depth-to-width ratio 1:2 for $Re' = 500$ and 1000. The size of left bottom corner vortex increases substantially and drifts further off the bottom wall as Re' increases from 500 to 1000, while the positions and strengths of the right bottom corner vortex and the primary vortex are weakly affected by Re'. The present results (left column) are in good agreement with the streamlines (right column) obtained previously by Cheng and Hung [4].

Fig. 4 shows contour lines of the stream-function (black lines) and the vortices identified by the λ_2 method (blue lines) proposed by Jeong and Hussain [27] for steady lid-driven rectangular cavity flow with $Re' = 1000$. The λ_2 method identifies the primary vortex and the bottom corner vortices, which are also visualized by closed streamlines. However, the flow at the upper-left corner is also identified as a vortex by the λ_2 method whereas the streamlines are not closed in this case, thus demonstrating the complexity of vortex identification. In this paper, the stream function is applied to identify the flow patterns for both the steady and oscillatory lid-driven cavity flow following the practice of previous works [4,14,28,29].

4.2. Oscillatory lid-driven cavity flow

Simulations of the flow within an oscillatory lid-driven square cavity have been compared with previous numerical results [13, 14,26]. Fig. 5 shows the center-line velocity profiles $u(0.5, y)$ and $v(x, 0.5)$ for $Re = 100$, 400 and 1000 at different times (indicated in the legend) for $\omega' = St/Re = 1$. The present results are in good agreement with those of Iwatsu et al. [13] while showing some deviation from the results obtained by Liu [26], especially for $Re = 1000$. The boundary layer thickness beneath the moving lid decreases as the Reynolds number (and consequently the Stokes number) increases. This is consistent with laminar boundary layer theory (i.e. Stokes second problem described in Schlichting et al. [30]) and also with the findings by Duck [31].

Simulations of the flow within an oscillatory lid-driven rectangular cavity have been compared with the experimental results previously obtained by Vogel et al. [19]. They conducted an experimental investigation of the two-dimensional and three-dimensional flow regimes in an oscillatory lid-driven cavity with depth-to-width ratio 1:2 and spanwise aspect ratio 1:19.4 for a wide range of Re and St. Here the bottom was moving while the upper lid was fixed. Experimental results for the two-dimensional flow regime are compared with the present results by contours of the z-component of the vorticity ($\Omega_z = \partial v/\partial x - \partial u/\partial y$) for $Re = 166$, 332, 498 and 747 for a fixed $St = 53$ as shown in Fig. 6. Here the left column shows Ω_z obtained from the measurements, while the right column shows Ω_z obtained by the present numerical simulations. It should be noted that Vogel et al. [19] did not present the values of the contours of Ω_z obtained from the measurements, and thus values of the contours in the numerical

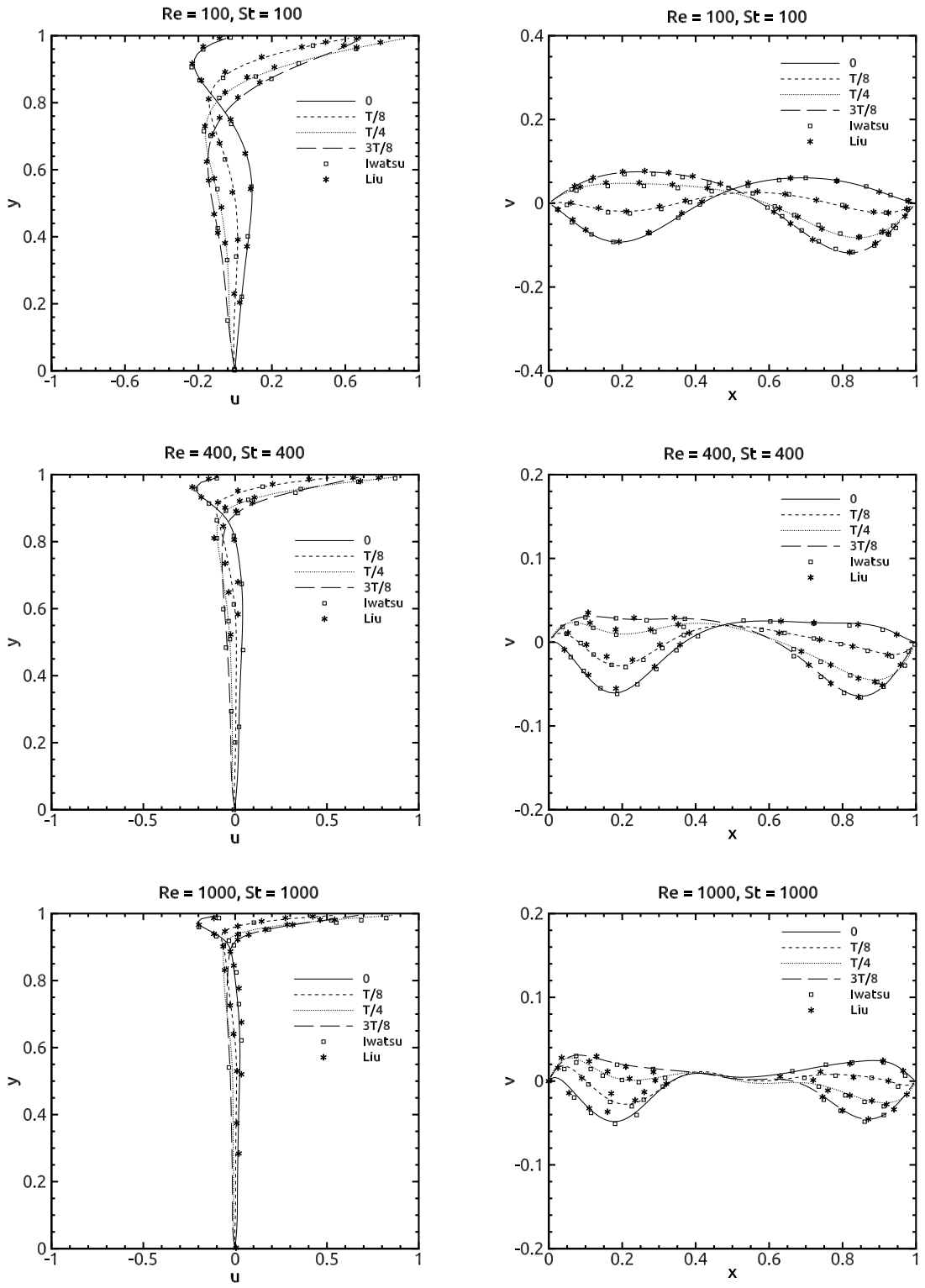

Fig. 5. Comparisons of $u(0.5, y)$ and $v(x, 0.5)$ between the present results and those obtained by Iwatsu et al. [13] and Liu [26] for the oscillatory lid-driven cavity flow.

simulations have been chosen (as best fit by eye) to match the measurements. Fig. 6 shows that the qualitative agreement is fair; the experimental measurements may deviate from the numerical simulations due to the uncertainty of the measured vorticity. Moreover, the present contours are similar to the numerical results (not shown here) presented by Vogel et al. [19].

5. Results and discussion

5.1. Basic flow patterns

Fig. 7 shows streamline contours for $Re = 125$ and $St = 23$ for the first half-cycle of oscillation. At $t = 0$, where the lid velocity is at its largest during the oscillation cycle (the lid

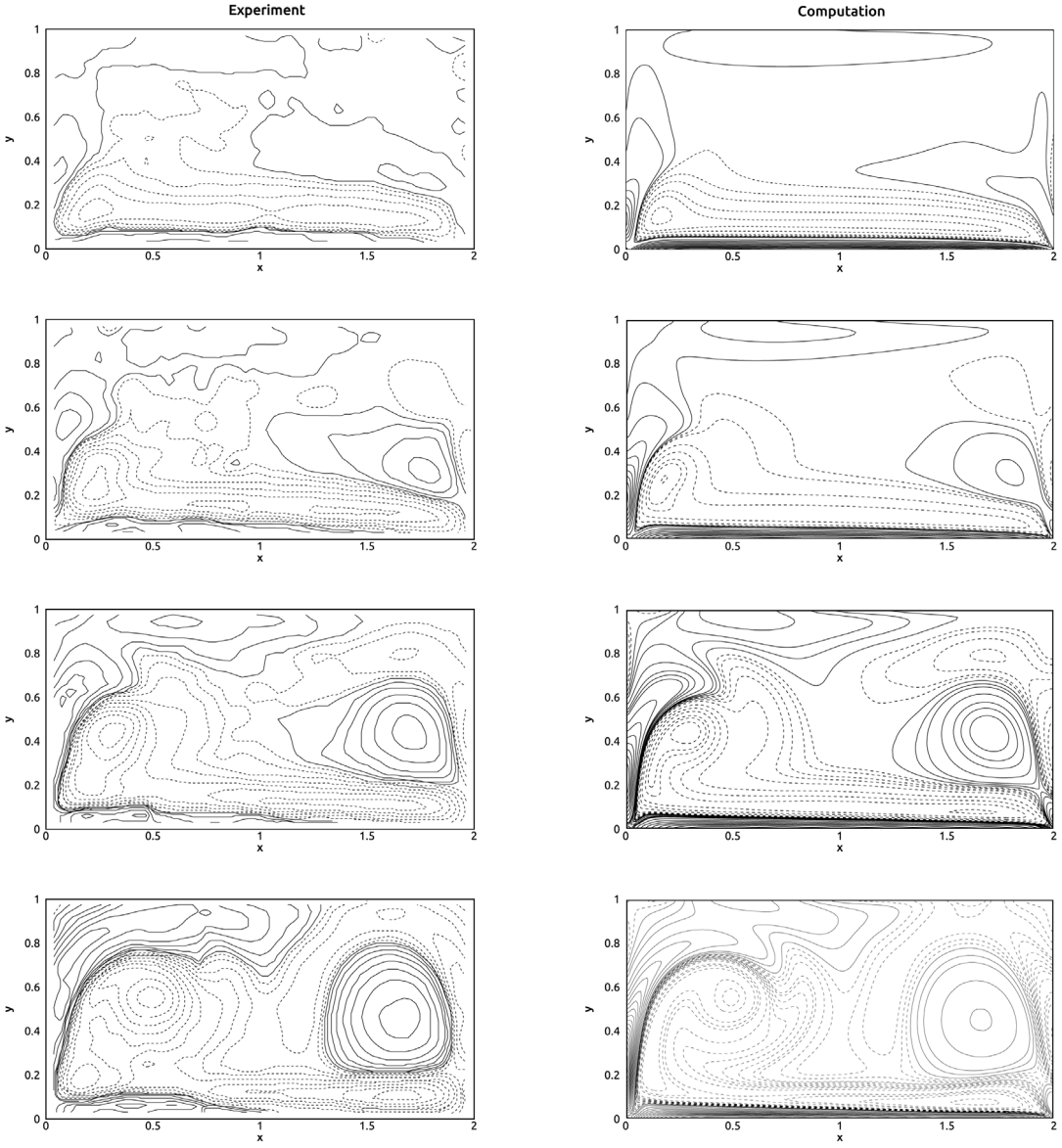

Fig. 6. Comparisons between predictions (right column) and measurements (left column) by Vogel et al. [19] for contours of Ω_z at Re = 166, 332, 498 and 747 (from top to bottom) and St = 53. All the data are for phase t = 0. Dashed and solid lines indicate negative values and positive values, respectively.

is moving towards the right), the cavity is almost completely occupied by the clockwise primary vortex (*CPV*), and the flow here is qualitatively similar to a steady lid-driven cavity flow. As the lid velocity decreases ($t = 0.2$), flow separation and reattachment cause a bottom left corner vortex (*BLCV*), and a bottom right corner vortex (*BRCV*) as well as a left wall vortex (*LWV*). These three vortices grow in size and strength and the weaker left wall vortex becomes encircled by the stronger bottom left corner vortex from $t = 0.20$ to 0.22, and then ($t = 0.25$) they merge (*LWV* + *BLCV*) to an anti-clockwise vortex which grows with time, while the clockwise primary vortex shrinks. As the lid starts moving towards the left ($t = 0.3$), the flow driven by the lid (rolls down at the upper left corner) forms an anti-clockwise elongated upper left corner vortex (*ULCV*) confined by the clockwise primary vortex and the (*LWV* + *BLCV*) vortex. Furthermore, an anti-clockwise upper right corner vortex (*URCV*) appears due to the interaction between the flow moving with the lid and the clockwise primary vortex. These two vortices near the lid push the clockwise primary vortex away downwards from the lid, while the (*LWV* + *BLCV*) vortex pushes the clockwise primary vortex towards the right. As a result, from $t = 0.3$ to $t = 0.45$ the clockwise primary vortex shrinks gradually, and the (*LWV* + *BLCV*) vortex merges with the upper left corner vortex while the vortices at the upper right corner (*URCV*) and at the bottom right corner (*BRCV*) erode rapidly. Finally ($t = 0.5$), the clockwise primary vortex vanishes, and the flow becomes anti-symmetric compared with the flow field at $t = 0$. In the flow shown in Fig. 7 the clockwise primary vortex exists without the simultaneous presence of the anti-clockwise primary vortex (and vice versa) for a small interval of the oscillation cycle where the magnitude of the lid velocity is largest, i.e. at t = n/2 where n is the number of cycles. The flow pattern which fulfills this criterion will hereafter be denoted flow pattern *A*.

Fig. 8 shows further details (close-up) of the merging of the left wall vortex (*LWV*) and the bottom left corner vortex (*BLCV*), previously shown in Fig. 7. At $t = 0.20$, the flow separates at $(x, y) = (0, 0.4)$ and reattaches at (0, 0.52) at the left wall, forming the small left wall vortex. As time increases, the separation point moves downward and meets at $t = 0.205$; the attachment point of the bottom left corner vortex is located at (0, 0.3). From $t =$

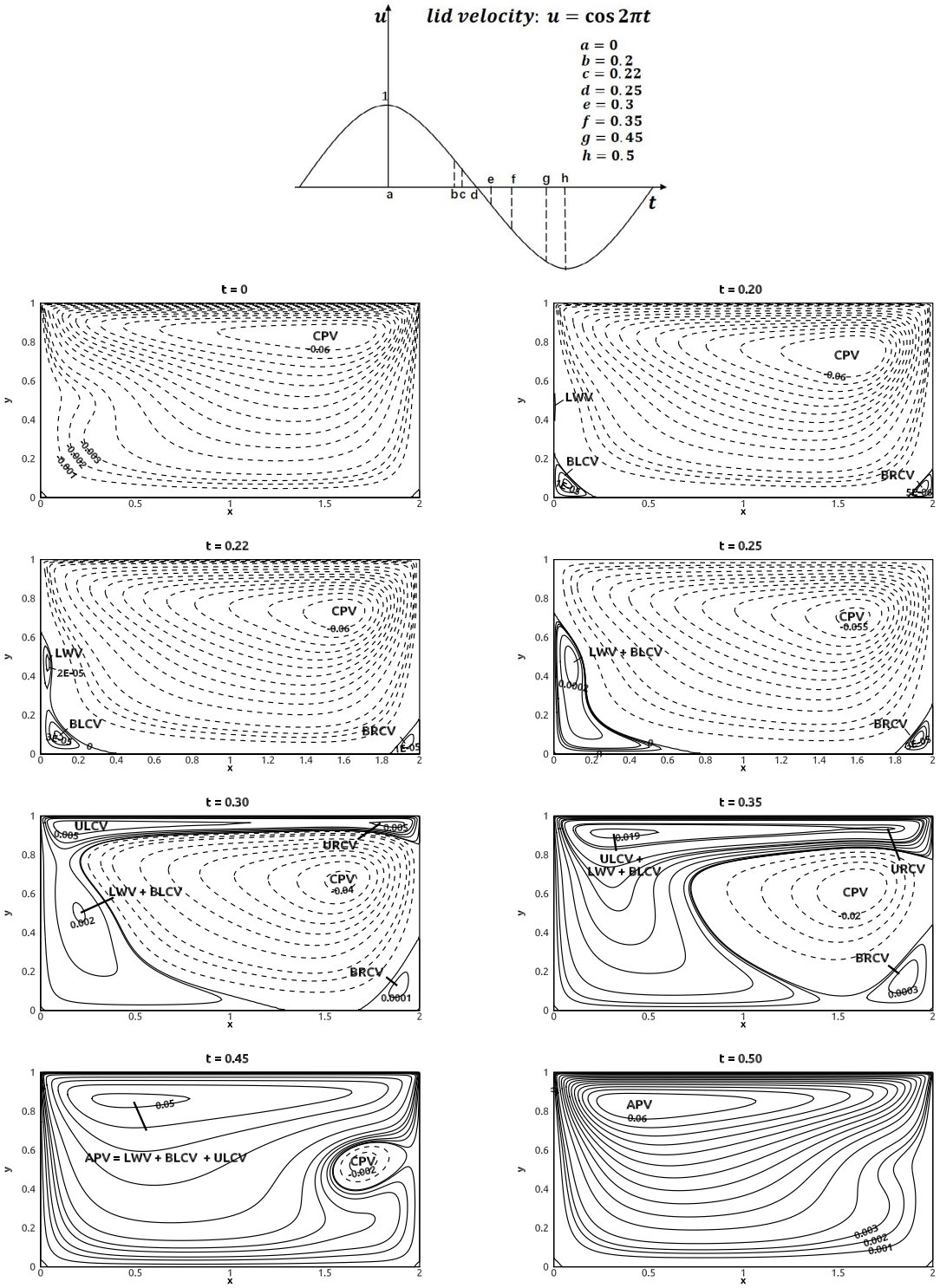

Fig. 7. Streamline contours for flow pattern A at $Re = 125$ and $St = 23$; for contours with values from -0.06 to 0.06, the difference in value between two adjacent contour lines is 0.005, for contours with values from -0.005 to 0.005, the difference in value between two adjacent contour lines is 0.001, for contours with values from 0.0001 to 0.0004, the difference in value between two adjacent contour lines is 0.0001, for contours with values from 1e-05 to 3e-05, the difference in value between two adjacent contour lines is 1e-05. Dashed and solid lines indicate negative values and positive values, respectively.

0.22 to $t = 0.23$, these two vortices have nearly equal strength, and grow in size by vorticity diffusion. Additionally, they grow in strength due to the positive vorticity near the walls but they do not rotate about each other due to the presence of the walls. It appears that the left wall vortex grows faster than the bottom left corner vortex, and the merging of them is qualitatively similar to that of an unequal co-rotating vortex pair; the weaker bottom left corner vortex deforms rapidly while the stronger left wall vortex gradually dominates with core detrainment (from $t = 0.23$ to $t = 0.24$), and finally they merge ($t = 0.25$) to form the ($LWV + BLCV$) vortex. Fig. 9 displays another close-up of Fig. 7, showing the evolution of the two co-rotating vortices at the upper left corner ($ULCV$) and at the upper right corner ($URCV$) as well as the already merged vortex ($LWV + BLCV$). As the lid

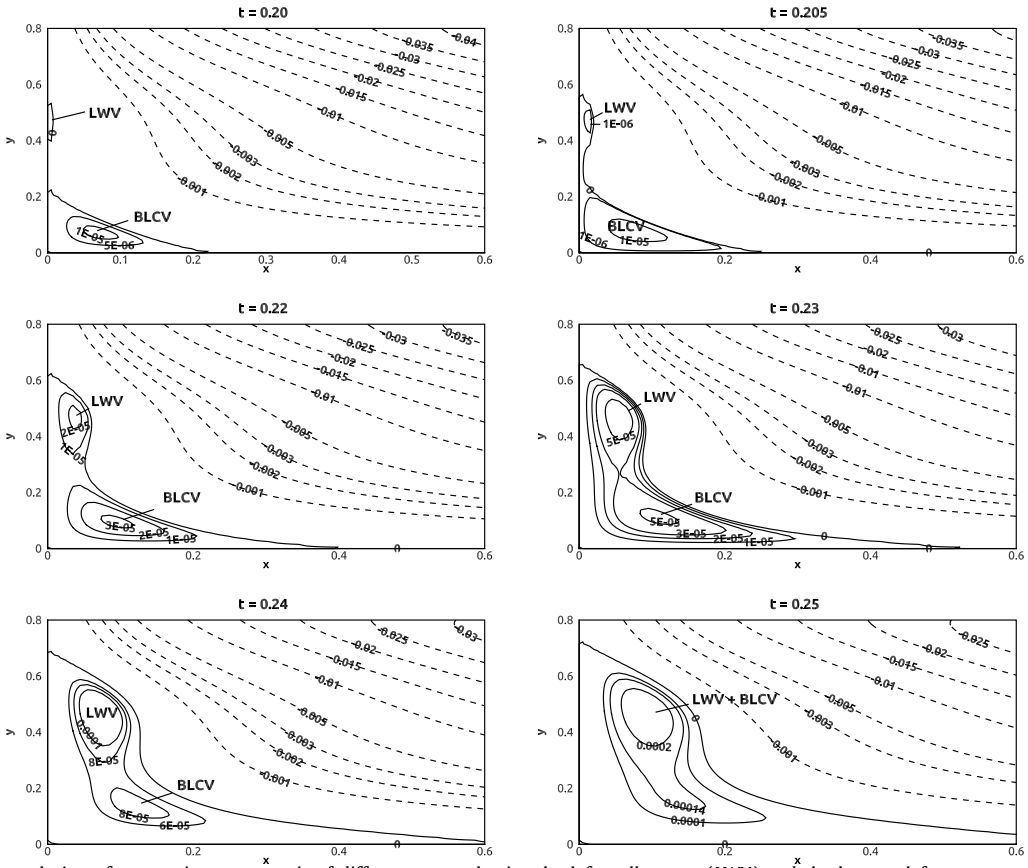

Fig. 8. The evolution of co-rotating vortex pair of different strengths, i.e. the left wall vortex (*LWV*) and the bottom left corner vortex (*BLCV*).

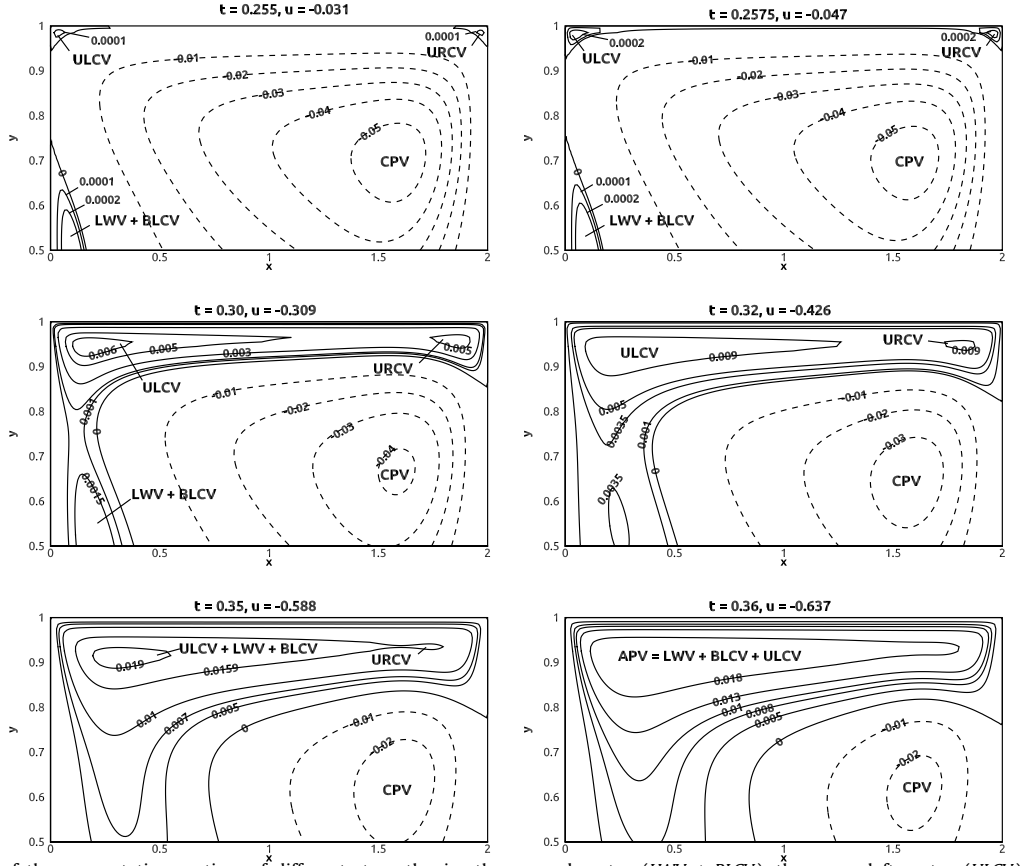

Fig. 9. The evolution of three co-rotating vortices of different strengths, i.e. the merged vortex (*LWV* + *BLCV*), the upper left vortex (*ULCV*) and the upper right corner vortex (*URCV*).

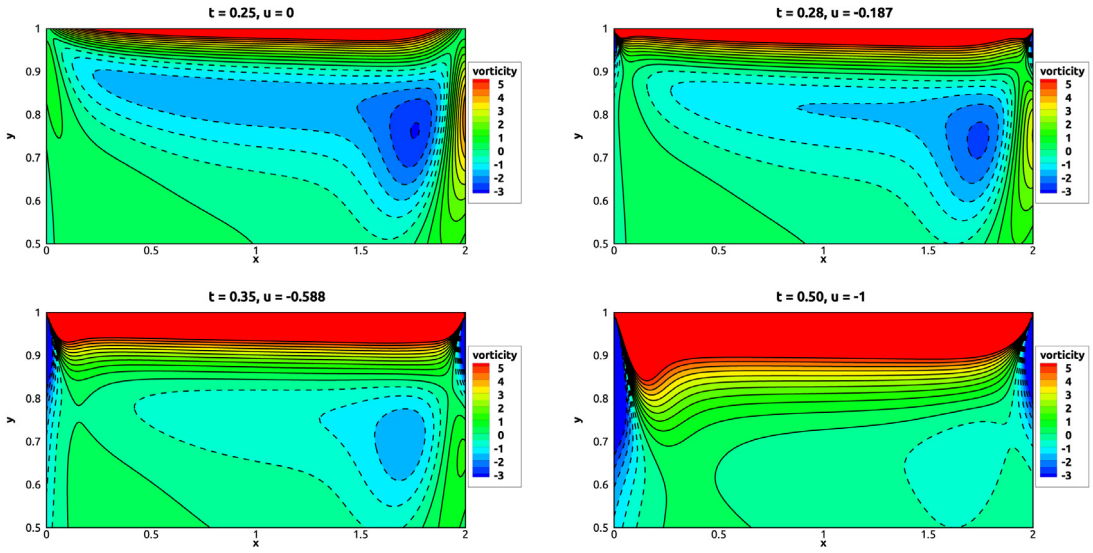

Fig. 10. Streamline contours (bold black lines) and vorticity contours Ω_z from $t = 0.25$ to $t = 0.50$ for $St = 23$ with $Re = 125$.

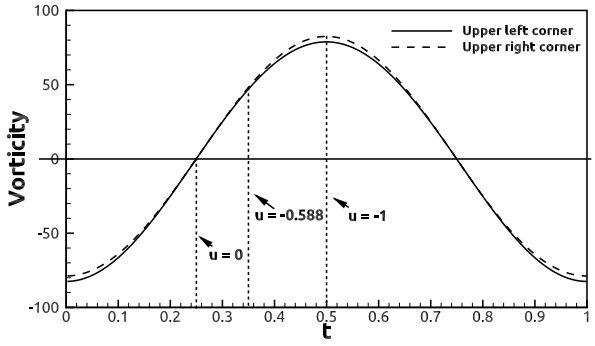

Fig. 11. Time history of Ω_z monitored at the center of the cells nearest the upper corners through one oscillation cycle for $Re = 125$ and $St = 23$.

moves towards the left ($t = 0.255$), two anti-clockwise vortices are formed at the upper left and right corners, respectively. Then at $t = 0.2575$ they grow and meet beneath the lid. The weaker upper right corner vortex grows in strength (from $t = 0.30$ to $t = 0.32$) and erodes gradually without the core detrainment of the stronger upper left corner vortex (from $t = 0.35$ to $t = 0.36$), i.e. these two vortices do not merge. However, the merging between the weaker ($LWV+BLCV$) vortex and the stronger ($ULCV$) vortex appears to be present; the core detrainment occurs in the stronger vortex as the weaker one moves towards it (from $t = 0.30$ to $t = 0.32$), and the merging occurs ($t = 0.35$), forming the anti-clockwise primary vortex ($APV = LWV + BLCV + ULCV$).

The shear layer beneath the moving lid has been further investigated by visualizing the vorticity contours Ω_z in Fig. 10 within the time interval $t = 0.25$ to 0.50 (the corresponding streamlines are shown in Fig. 7). Due to the oscillation cycle, some vorticity remains beneath the lid when the lid velocity is zero (at $t = 0.25$). As the lid moves from the right towards the left, the thickness of the shear layer beneath the lid increases both with time and along the lid. It is observed that as the shear layer beneath the lid becomes thicker, the corner vorticity singularities shown in Fig. 10 (shown by the contraction of the vorticity contours towards the upper corners) become more visible. This is further visualized in Fig. 11, showing the vorticity evaluated at the center of the cell nearest to the upper left and right corners through the oscillation cycle. The magnitude of the vorticity Ω_z on the bisection of the singular corner and in the immediate vicinity of the corner is small as the lid velocity is zero (at $t = 0.25$ and $t = 0.75$), which is consistent with the observation from Fig. 10 for $t = 0.25$. As the lid moves towards the left in the time interval from $t = 0.25$ (where $u = 0$) to $t = 0.35$ (where $u = -0.588$), the magnitude of the near-corner vorticities increases. As the lid velocity increases further, the magnitude of the vorticity near the right corner becomes slightly larger than that near the left corner with the maximum deviation observed at $t = 0.50$ (where $u = -1$); and vice versa for u = 1. Some further aspects of the upper corner singularities will be discussed below in Section 5.2.

Fig. 12 shows streamline contours for $Re = 200$ and $St = 23$ for the first half-cycle of oscillation. Here, a remaining part of the anti-clockwise primary vortex (APV) from the previous half-cycle of oscillation is present at the left wall; this vortex does not completely vanish at any instance of the oscillation cycle as it does for flow pattern A shown in Fig. 7. Except from this, the vortex dynamics is similar to that of flow pattern A; the remaining part of the anti-clockwise primary vortex merges gradually with the bottom left corner vortex ($t = 0.24$) in the same manner as the left wall vortex does in flow pattern A; the upper left and right corner vortices are formed beneath the lid ($t = 0.3$), and from $t = 0.34$ to $t = 0.5$ the upper left corner vortex merge gradually with the ($APV+BLCV$) vortex, forming the anti-clockwise primary vortex while the upper left corner vortex and the upper right corner vortex erode. However, a small part of the clockwise primary vortex remains as the next half-cycle of oscillation starts. The flow pattern exhibiting this behavior is denoted flow pattern B.

Fig. 13 shows streamline contours for $Re = 350$ and $St = 23$ for the first half-cycle of oscillation. At $t = 0$, the remaining part of the anti-clockwise primary vortex is so large that it separates the bottom left corner vortex from the clockwise primary vortex, resulting in a bottom left corner vortex ($BLCV'$) with a clockwise rotation instead of the anti-clockwise rotation observed in flow patterns A and B. As the lid velocity decreases, this clockwise bottom vortex ($BLCV'$) decreases gradually in size and strength (from $t = 0.04$ to $t = 0.24$) and finally vanishes ($t = 0.24$). The merging of $ULCV$ and APV, the erosion of $URCV$ and the decay of the clockwise primary vortex with time are qualitatively similar to those observed in flow patterns A and B, except that the bottom right corner vortex does not erode ($t = 0.5$). This is because the bottom right corner vortex here is isolated from the anti-clockwise primary vortex by the remaining clockwise primary vortex. Consequently, the flow here carries two vortices (the

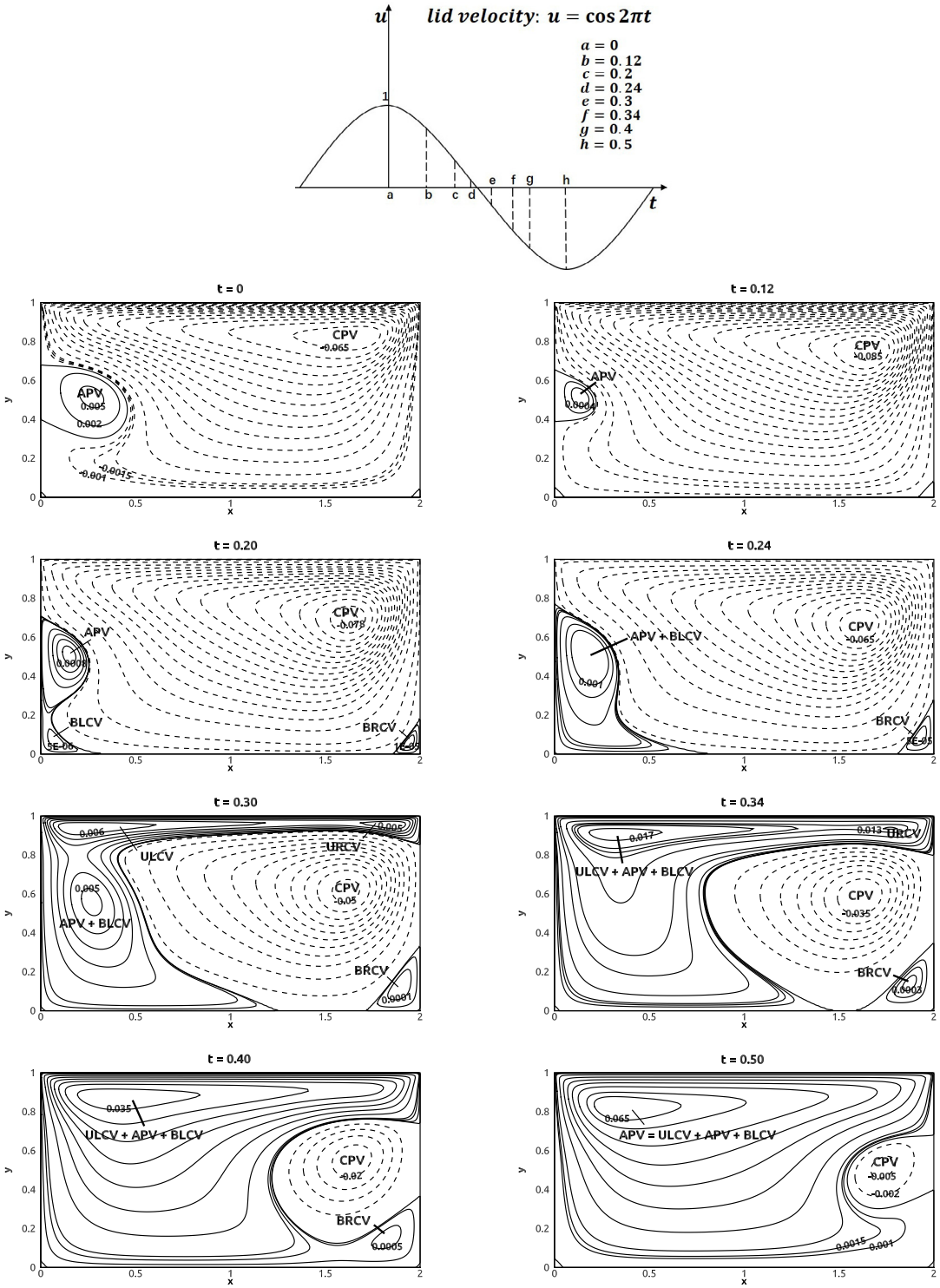

Fig. 12. Streamline contours for flow pattern *B* at $Re = 200$ and $St = 23$; for contours with values from -0.085 to 0.065, the difference in value between two adjacent contour lines is 0.005, for contours with values from -0.005 to 0.005, the difference in value between two adjacent contour lines is 0.001, for contours with values from 0.0002 to 0.0008, the difference in value between two adjacent contour lines is 0.0002, for contours with values from 1e-05 to 5e-05, the difference in value between two adjacent contour lines is 2e-05, for contours with values from 1e-06 to 5e-06, the difference in value between two adjacent contour lines is 4e-06. Dashed and solid lines indicate negative values and positive values, respectively.

clockwise primary vortex and the bottom right corner vortex) between the two successive half-cycles of oscillation. The flow exhibiting this behavior is denoted flow pattern *C*.

Fig. 14 shows streamline contours for $Re = 550$ and $St = 23$ for the first half-cycle of oscillation. At $t = 0$, the cavity is occupied by the clockwise primary vortex as well as the remaining part of the anti-clockwise primary vortex and the clockwise bottom left corner vortex. As the clockwise primary vortex core approaches the bottom, a closed region of recirculation appears on the wall, leading to the formation ($t = 0.16$) of an anti-clockwise bottom vortex (BV) which does not appear in flow patterns *A*-*C*. This behavior is qualitatively similar to the observations of Walker

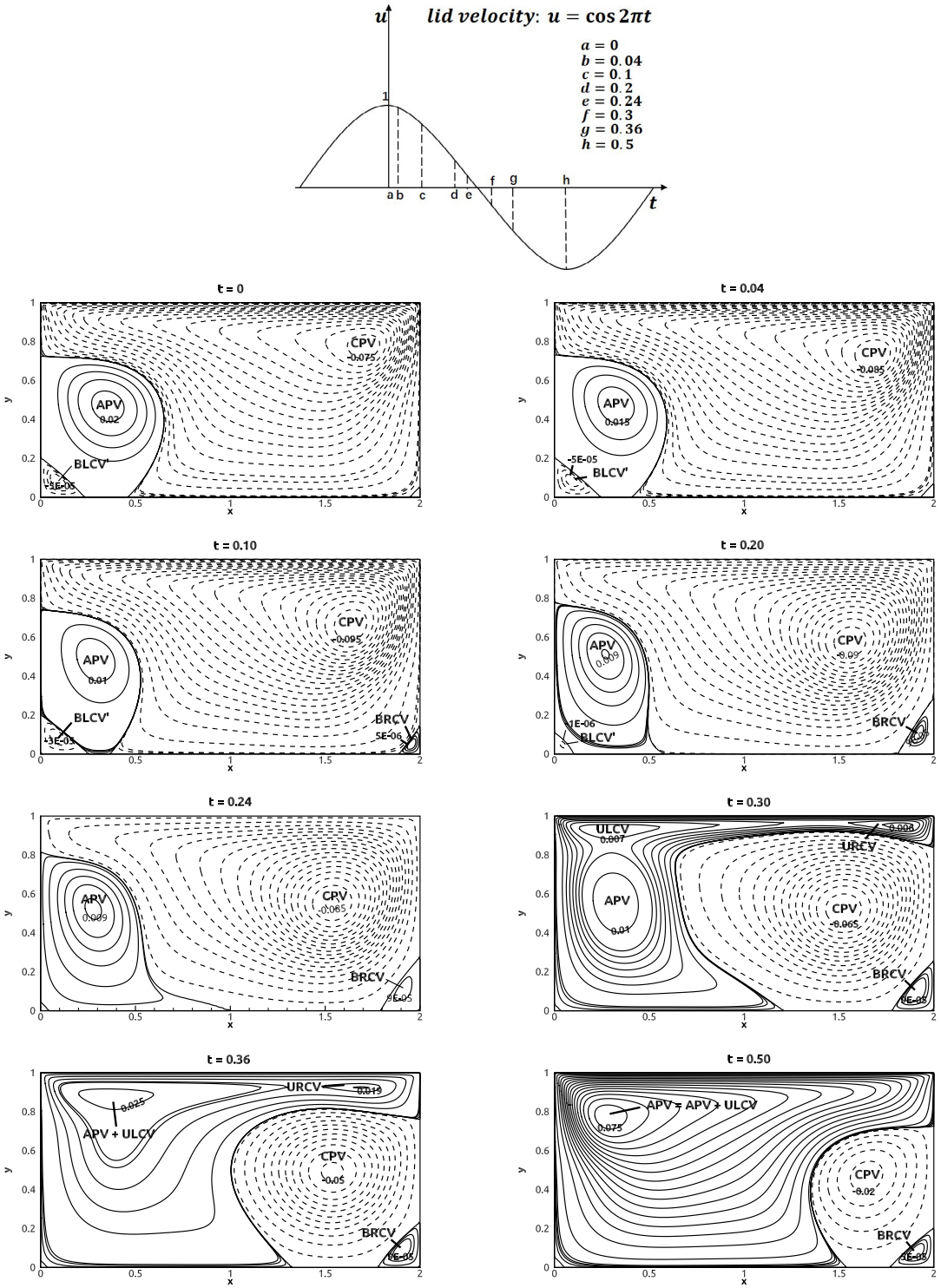

Fig. 13. Streamline contours for flow pattern C at $Re = 350$ and $St = 23$; for contours with values from -0.095 to 0.075, the difference in value between two adjacent contour lines is 0.005, for contours with values from -0.001 to 0.009, the difference in value between two adjacent contour lines is 0.002, for contours with values from $-5e\text{-}05$ to 9e-05, the difference in value between two adjacent contour lines is 2e-05, for contours with values from $-1e\text{-}06$ to 5e-06, the difference in value between two adjacent contour lines is 2e-06. Dashed and solid lines indicate negative values and positive values, respectively.

et al. [32] who found that as a primary vortex ring approaches a solid wall, a wall eddy with opposite vorticity will be present in the close vicinity of the wall. The interaction between the co-rotating vortex pair (BV and APV) is described in further details in Fig. 15; flow separation and reattachment occur between (x, y) = (0.725, 0) and (0.84, 0) at the bottom for $t = 0.1525$, forming the bottom vortex (BV), which grows gradually ($t = 0.16$) due to the vorticity diffusion and meets ($t = 0.1625$) with the primary vortex (APV), and is eventually ($t = 0.22$) destroyed by the stronger primary vortex (APV) which remains relatively unaffected as shown in Fig. 14 (from $t = 0.2$ to $t = 0.22$). The flow state which includes the bottom vortex is denoted flow pattern D.

Further details of the vortex generating mechanisms are obtained by contours of Ω_z shown in Fig. 16. Here the vorticity

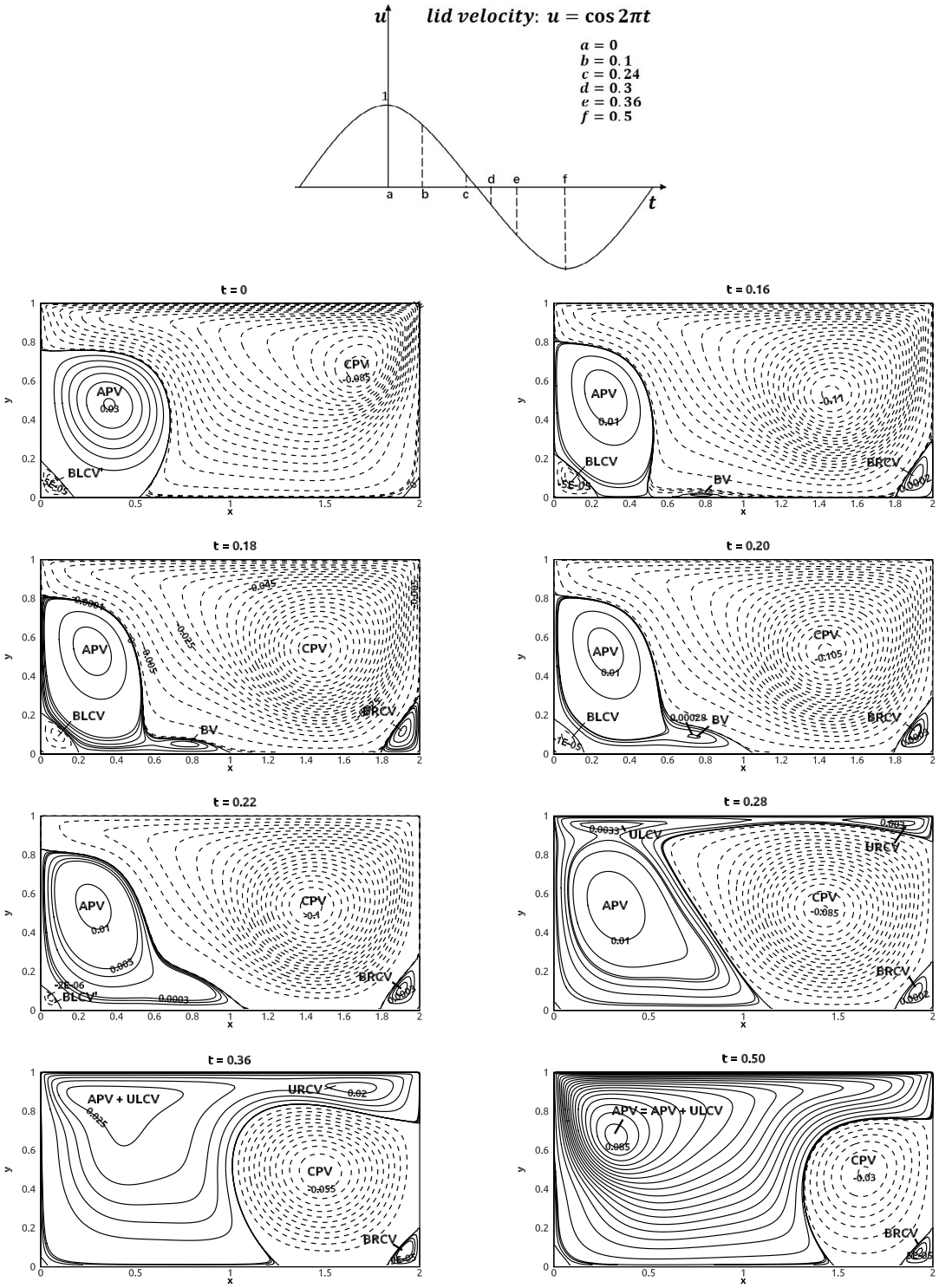

Fig. 14. Streamline contours for flow pattern D at $Re = 550$ and $St = 23$; for contours with values from -0.11 to 0.085, the difference in value between two adjacent contour lines is 0.005, for contours with values from -0.001 to 0.003, the difference in value between two adjacent contour lines is 0.001, for contours with values from 0.0001 to 0.0003, the difference in value between two adjacent contour lines is 0.0001, for contours with values from $-5e\text{-}05$ to 5e-05, the difference in value between two adjacent contour lines is 2e-05, Dashed and solid lines indicate negative values and positive values, respectively.

contours for $t = 0$ and $t = 0.16$ corresponds to the streamlines (for $t = 0$ and $t = 0.16$) shown in Fig. 14. The generation of vorticity along the oscillating lid as well as the vorticity which occurs due to the vertical wall are clearly visualized. As pointed out by Ovando et al. [15] the vortex shedding (Fig. 16, $t = 0.16$) due to the rolling down of the vortex sheets at the right wall follows the qualitative behavior of a vortex approaching a wall perpendicularly, first predicted by Peace and Riley [33] and observed experimentally by Walker et al. [32] and Allen and Chong [17]. As the vortex is approaching the wall (Fig. 16, $t = 0$), a region with opposite vorticity sign occurs between the vortex and the wall, causing the vortex to rebound from the wall (Fig. 16, $t = 0.16$); this can also be seen from Fig. 14 ($t = 0$ and $t = 0.16$). These mechanisms are similar to those previously

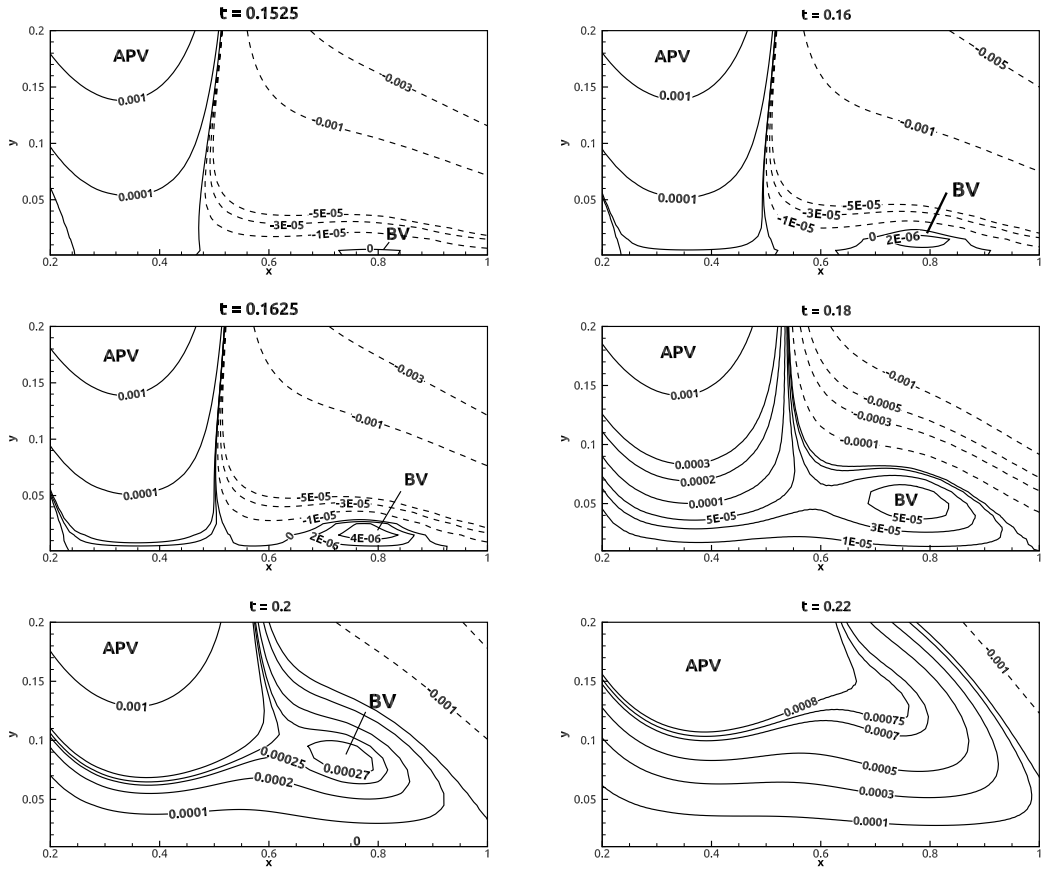

Fig. 15. The merging process of the asymmetric vortex pair, i.e. the anti-clockwise bottom vortex (*BV*) and primary vortex (*APV*).

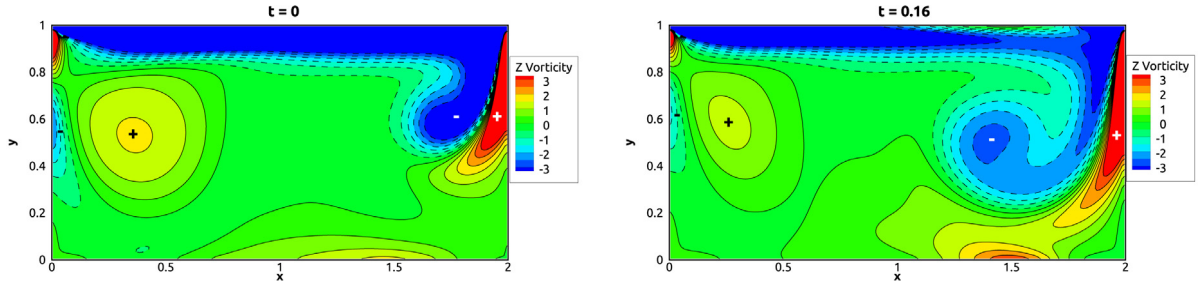

Fig. 16. Contours of Ω_z for $Re = 550$ and $St = 23$; dashed and solid lines indicate negative values and positive values, respectively.

visualized by Ovando et al. [15] for a rectangular cavity with two simultaneously oscillating vertical walls.

5.2. Effect of upper corner vorticity singularity

Now the flow in the vicinity of the upper left and right corners where the vorticity is singular will be discussed. These singularities cause numerical challenges, making it more difficult to obtain an accurate numerical solution in the close vicinity of the upper corners. For spectral methods, the global nature of the trial function in conjunction with the upper corner singularities leads to spurious oscillations. This is overcome by combining the trial functions with local analytic solutions based on asymptotic series expansions in terms of the local Reynolds number, which is small due to the small flow velocity near the upper corner [24,34]. Also for finite difference, finite volume and finite element methods, the upper corner singularities lead to numerical inaccuracies. Bruneau and Saad [25] applied a finite difference method showing that for a steady lid-driven square cavity flow for $Re = 1000$ and 5000, grid convergence was obtained for the total kinetic energy $E = \frac{1}{2}\oint_S \|U\|^2 dS$ (where S is the computation domain, and Ω_z is evaluated at the cell center), whilst grid convergence could not be obtained for neither the enstrophy $Z = \frac{1}{2}\oint_S \|\Omega_z\|^2 dS$ nor the palinstrophy $P = \frac{1}{2}\oint_S \|\nabla\Omega_z\|^2 dS$. As pointed out by Bruneau and Saad [25], this is caused by the infinite velocity gradients in the corners, causing the enstrophy and the palinstrophy to approach infinity as the grid cell size approaches zero. Similar results are obtained in the present work for oscillating lid-driven cavities. Fig. 17 shows the total energy E for $St = 23$ and $Re = 550$ through the oscillation cycle obtained from both a resolution of 200×100 and 400×200 grid cells (in the x and y direction, respectively) with a maximum deviation of 0.8% between the two grid resolutions. However, for the enstrophy (also shown in Fig. 17), the corresponding maximum deviation is 5.9%. This result is qualitatively similar to those by Bruneau and Saad [25] who obtained corresponding deviations from 4%–8% and from 4%–10% for steady lid-driven flow with $Re = 1000$ and 5000, respectively. Although grid convergence of both the enstrophy

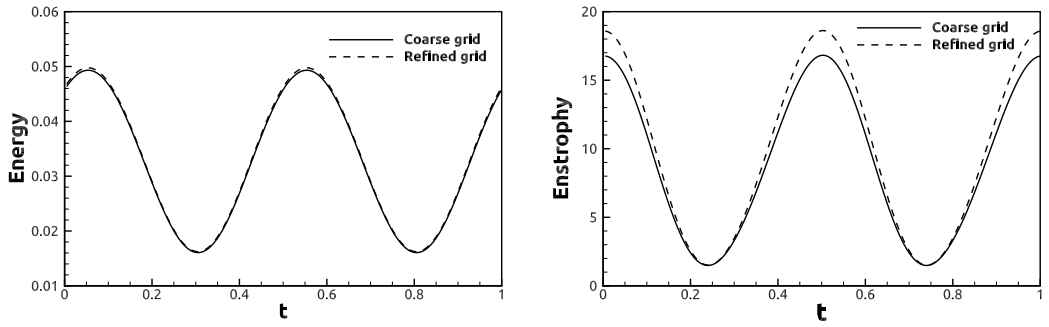

Fig. 17. Time history of energy (left) and enstrophy (right) over one oscillation cycle for $Re = 550$ and $St = 23$.

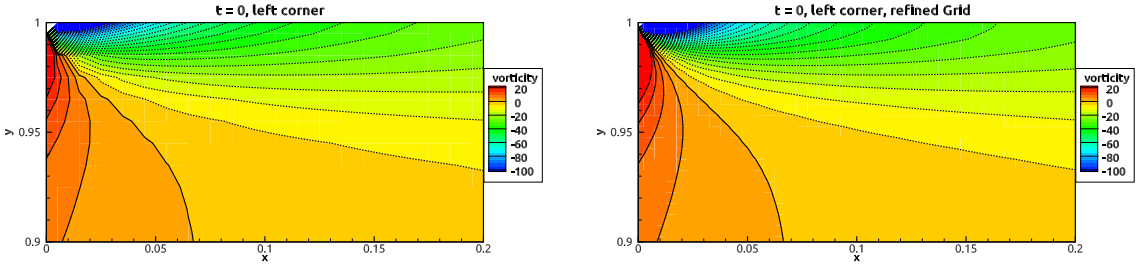

Fig. 18. Close-up of Ω_z for the upper left corner at grid resolution 200 × 100 (left) and refined grid resolution 400 × 200 (right) for $St = 23$ with $Re = 550$.

and the palinstrophy can be obtained by letting the lid velocity approach zero locally at the corners [25], this case is not relevant for comparison with laboratory measurements, as pointed out by Shankar and Deshpande [5]. A close-up of the vorticity contours in the vicinity of the left corner is shown in Fig. 18 for the two different resolutions of 200 × 100 and 400 × 200 grid cells; the difference between the contour lines obtained from the two grid resolutions is small. Although the upper corner singularities affect the accuracy of the numerical solution, particularly in the close vicinity of the corners, the vorticity is adequately resolved in the present simulations, as demonstrated in Fig. 18.

5.3. Distribution of the basic flow patterns in (St, Re)-space

Fig. 19 shows the distribution of flow patterns *A*-*D* in the (*St*, *Re*)-space; the full line denotes the transition between 2*D* and 3*D* flow [19]. More than 400 numerical simulations with *Re* from 10 to 875 and with *St* from 23 to 53 have been conducted to map out the regions in the (*St*, *Re*)-space of the flow patterns represented by the dashed lines in Fig. 19. For a given *St* number, the flow patterns *A*-*D* appear sequentially as *Re* increases, showing that the transition between the different flow patterns strongly depends on *Re*. Furthermore, as *St* increases, the *Re* for the transition between different flow patterns increases. This is because an increase in *St* for a given *Re* leads to less time for the extrema of the stream function to grow and for the primary vortex center to move away from the lid. Consequently, a higher *Re* is required to maintain the same flow pattern. This effect appears to be stronger for the flow pattern *D* than for the flow pattern *A*. It appears that the transition between the different flow patterns (i.e. the dashed lines) is given by an approximately linear relation between *Re* and *St*.

Fig. 20 shows the scaled drag force (defined as $\int_0^2 \frac{\partial u}{\partial y}|_{y=1} dx$) beneath the moving lid through one oscillation cycle for $St = 23$ and for $Re = 125$, 200, 350 and 550; i.e. for the flow patterns *A*-*D*. It appears that an increase in *Re* leads to a moderate growth and phase shift of the drag force. Fig. 21(a) shows the phase shift between the lid oscillation velocity and the drag force on the lid for $Re = 10$, 125, 250 and 490 and for $St = 23$, 28, 33,

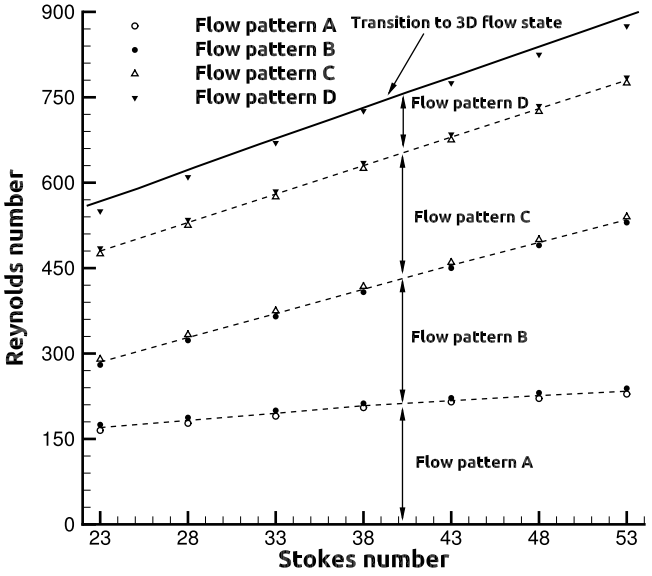

Fig. 19. Basic flow patterns $A - D$ of the two-dimensional oscillatory lid-driven cavity within (*St*, *Re*)-space.

38, 43, 48 and 53. The phase shift increases monotonically as *St* increases whereas an increase of *Re* results in lower phase shifts. The maximum phase shift is 30° (for $St = 53$ and $Re = 10$), which is considerably smaller than the 45° phase shift obtained from the Stokes' classical second problem. Fig. 21(b) shows the horizontal velocity component along the vertical center-line of the cavity for $t = 0.2$ and 0.6 for $St = 53$ and for $Re = 10$ and 490. The flow driven by an infinite plate (Stokes solution) is given for comparison. As *Re* decreases, the near-lid velocity becomes more similar to the Stokes solution. This is consistent with the observation in Fig. 21(a) showing that the flow with smallest *Re* and largest *St* exhibits the phase shift (30°) between the drag force and the lid velocity which is closest to that from the Stokes solution (45°). However, farther away from the lid, the velocity

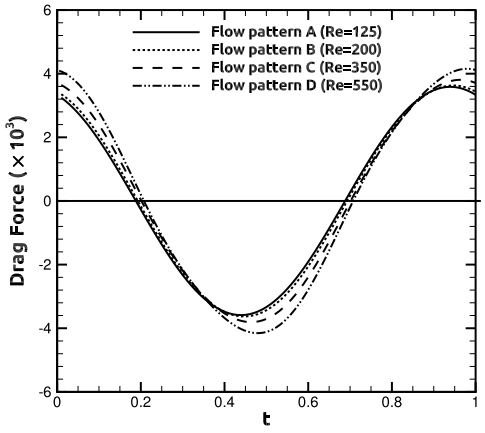

Fig. 20. The drag force beneath the moving lid at $St = 23$ and for $Re = 125$, 200, 350 and 550; i.e. for the flow patterns *A-D*.

component obtained for $Re = 490$ is closer to Stokes solution than that obtained for $Re = 10$.

6. Summary and conclusions

This paper provides a detailed investigation of the vortex dynamics in the oscillatory lid-driven cavity with depth-to-width ratio 1:2, covering a wide range of Reynolds numbers and Stokes numbers where this flow is known to be in the two-dimensional flow regime. The predictions have been successfully compared with previous numerical results for steady [4,22–25] and oscillatory [13,14,26] lid-driven cavity flows as well as with experimental results obtained by Vogel et al. [19] for oscillatory lid-driven cavity flows. Furthermore, the effect of the upper corner vorticity singularity is discussed: the total energy exhibits grid convergence while the enstrophy does not; these results are qualitatively similar to those obtained by Bruneau and Saad [25] for a steady lid-driven flow. Although the upper corner singularities affect the numerical accuracy of the predictions, it is demonstrated that the vorticity is adequately resolved.

It appears that the two-dimensional flow regime can be further divided into four flow patterns based on the vortex dynamics, which is visualized by streamline contours. The classification of these basic flow patterns can be summarized as follows:

- For flow pattern *A*, there is no transfer of vortices between each successive half-cycle of oscillation; this means that the clockwise primary vortex (generated by the lid moving towards the right) and the anti-clockwise primary vortex (generated by the lid moving towards the left) are not present simultaneously at the end of each half-cycle of oscillation.
- For flow pattern *B*, a small part of the clockwise primary vortex remains as the next half-cycle of oscillation starts, and thus the flow carries the primary vortex between each successive half-cycle of oscillation when the lid velocity is largest.
- For flow pattern *C*, the flow carries two vortices between each successive half-cycle of oscillation. When the lid is moving towards the right, these two vortices consist of the anti-clockwise primary vortex and the clockwise bottom left corner vortex from the last half-cycle of oscillation.
- Flow pattern *D* is similar to flow pattern *C*, except the intermediate appearance of an additional bottom vortex during each half-cycle of oscillation.

These flow structures are unique functions of the Reynolds number and the Stokes number, and the pattern changes with these parameters. The increased forcing quantified by the Reynolds number and the Stokes number leads to finer flow structures and hence different flow patterns. If the frequency of oscillation is increased for a given Reynolds number, the extrema of the stream function have less time to grow and the center of the primary vortex has less time to move away from the lid. To compensate these effects, the amplitude has to be increased with increasing frequency to maintain the same flow pattern.

Declaration of competing interest

The authors declare that they have no known competing financial interests or personal relationships that could have appeared to influence the work reported in this paper.

Acknowledgments

We gratefully acknowledge the support for this research from the Department of Marine Technology, Norwegian University of Science and Technology, Norway and the China Scholarship Council (Grant no. 201506680058).

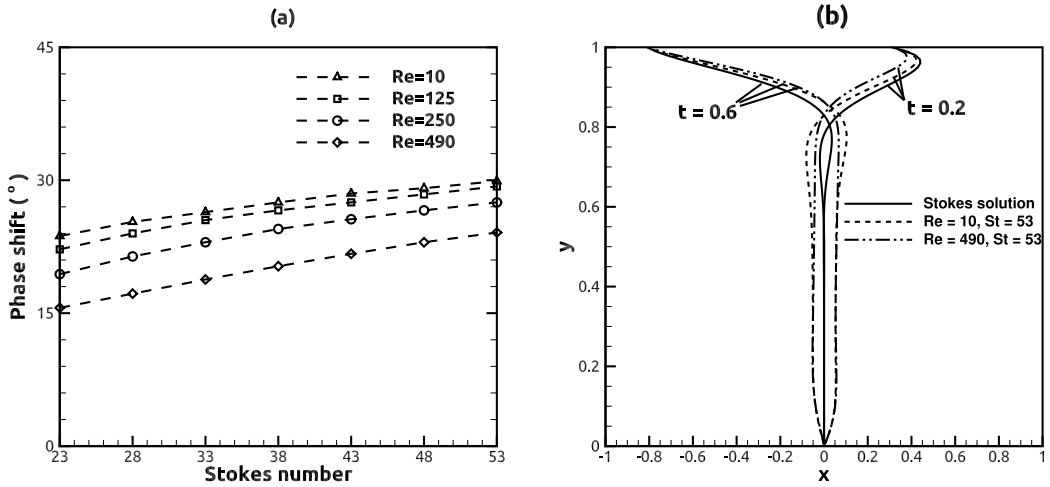

Fig. 21. (a): phase shift of the drag force on the moving lid at $Re = 10$, 125, 250 and 490 for $St = 23$, 28, 33, 38, 43, 48 and 53; (b): the horizontal velocity along the center-line of the cavity at $t = 0.2$ and 0.6 for $St = 53$ with $Re = 10$ and 490.

References

[1] T. Leweke, S. Le Dizes, C.H. Williamson, Dynamics and instabilities of vortex pairs, Annu. Rev. Fluid Mech. 48 (2016) 507–541.
[2] C. Josserand, M. Rossi, The merging of two co-rotating vortices: a numerical study, Eur. J. Mech. B Fluids 26 (6) (2007) 779–794.
[3] V. Sychev, Laminar separation, Fluid Dyn. 7 (3) (1972) 407–417.
[4] M. Cheng, K. Hung, Vortex structure of steady flow in a rectangular cavity, Comput. & Fluids 35 (10) (2006) 1046–1062.
[5] P. Shankar, M. Deshpande, Fluid mechanics in the driven cavity, Annu. Rev. Fluid Mech. 32 (1) (2000) 93–136.
[6] H. Moffatt, Singularities in fluid dynamics and their resolution, in: Lectures on Topological Fluid Mechanics, Springer, 2009, pp. 157–166.
[7] F. Pan, A. Acrivos, Steady flows in rectangular cavities, J. Fluid Mech. 28 (4) (1967) 643–655.
[8] J.H. Trowbridge, S.J. Lentz, The bottom boundary layer, Annu. Rev. Mar. Sci. 10 (2018) 397–420.
[9] C. Leong, J. Ottino, Experiments on mixing due to chaotic advection in a cavity, J. Fluid Mech. 209 (1989) 463–499.
[10] J.M. Ottino, Mixing, chaotic advection, and turbulence, Annu. Rev. Fluid Mech. 22 (1) (1990) 207–254.
[11] H.C. Kuhlmann, F. Romanò, The lid-driven cavity, in: Computational Modelling of Bifurcations and Instabilities in Fluid Dynamics, Springer, 2019, pp. 233–309.
[12] W. Soh, J.W. Goodrich, Unsteady solution of incompressible Navier-Stokes equations, J. Comput. Phys. 79 (1) (1988) 113–134.
[13] R. Iwatsu, J.M. Hyun, K. Kuwahara, Numerical simulation of flows driven by a torsionally oscillating lid in a square cavity, J. Fluids Eng. 114 (2) (1992).
[14] S.S. Mendu, P. Das, Fluid flow in a cavity driven by an oscillating lid - a simulation by lattice Boltzmann method, Eur. J. Mech. B Fluids 39 (2013) 59–70.
[15] G. Ovando, H. Juarez, G. Huelsz, E. Ramos, Vortex formation in a cavity with oscillating walls, Phys. Fluids 21 (2) (2009) 024101.
[16] R.J. Tabaczynski, D.P. Hoult, J.C. Keck, High Reynolds number flow in a moving corner, J. Fluid Mech. 42 (2) (1970) 249–255.
[17] J. Allen, M. Chong, Vortex formation in front of a piston moving through a cylinder, J. Fluid Mech. 416 (2000) 1–28.
[18] J.M. Lopez, A.H. Hirsa, Oscillatory driven cavity with an air/water interface and an insoluble monolayer: Surface viscosity effects, J. Colloid Interface Sci. 242 (1) (2001) 1–5.
[19] M.J. Vogel, A. Hirsa, J.M. Lopez, Spatio-temporal dynamics of a periodically driven cavity flow, J. Fluid Mech. 478 (2003) 197–226.
[20] J.J.F. Leung, A.H. Hirsa, H.M. Blackburn, F. Marques, J.M. Lopez, Three-dimensional modes in a periodically driven elongated cavity, Phys. Rev. E 71 (2) (2005) 026305.
[21] H.M. Blackburn, J.M. Lopez, The onset of three-dimensional standing and modulated travelling waves in a periodically driven cavity flow, J. Fluid Mech. 497 (2003) 289–317.
[22] U. Ghia, K.N. Ghia, C.T. Shin, High-re solutions for incompressible flow using the Navier-Stokes equations and a multigrid method, J. Comput. Phys. 48 (3) (1982) 387–411.
[23] F. Romano, H.C. Kuhlmann, Smoothed-profile method for momentum and heat transfer in particulate flows, Internat. J. Numer. Methods Fluids 83 (6) (2017) 485–512.
[24] O. Botella, R. Peyret, Benchmark spectral results on the lid-driven cavity flow, Comput. & Fluids 27 (4) (1998) 421–433.
[25] C.H. Bruneau, M. Saad, The 2D lid-driven cavity problem revisited, Comput. & Fluids 35 (3) (2006) 326–348.
[26] C.H. Liu, Numerical solution of three-dimensional Navier-Stokes equations by a velocity-vorticity method, Internat. J. Numer. Methods Fluids 35 (5) (2001) 533–557.
[27] J. Jeong, F. Hussain, On the identification of a vortex, J. Fluid Mech. 285 (1995) 69–94.
[28] K. Gustafson, K. Halasi, Vortex dynamics of cavity flows, J. Comput. Phys. 64 (2) (1986) 279–319.
[29] P. Shankar, R. Kidambi, J. Hariharan, Oscillatory eddy structure in a container, J. Fluid Mech. 494 (2003) 163–185.
[30] H. Schlichting, et al., Boundary Layer Theory, McGraw-Hill Book Company, 1979, pp. 135–149.
[31] P.W. Duck, Oscillatory flow inside a square cavity, J. Fluid Mech. 122 (1982) 215–234.
[32] J.D.A. Walker, C.R. Smith, A.W. Cerra, T.L. Doligalski, The impact of a vortex ring on a wall, J. Fluid Mech. 181 (1987) 99–140.
[33] A.J. Peace, N. Riley, A viscous vortex pair in ground effect, J. Fluid Mech. 129 (1983) 409–426.
[34] O. Botella, M. Forestier, R. Pasquetti, R. Peyret, C. Sabbah, Chebyshev methods for the Navier–Stokes equations: Algorithms and applications, Nonlinear Anal. TMA 47 (6) (2001) 4157–4168.